



**HAL**  
open science

# Fully decoupled time-marching schemes for incompressible fluid/thin-walled structure interaction

Miguel Angel Fernández, Mikel Landajuela

► **To cite this version:**

Miguel Angel Fernández, Mikel Landajuela. Fully decoupled time-marching schemes for incompressible fluid/thin-walled structure interaction. [Research Report] RR-8425, 2013. hal-00918498v2

**HAL Id: hal-00918498**

**<https://inria.hal.science/hal-00918498v2>**

Submitted on 9 Jan 2014 (v2), last revised 6 May 2015 (v4)

**HAL** is a multi-disciplinary open access archive for the deposit and dissemination of scientific research documents, whether they are published or not. The documents may come from teaching and research institutions in France or abroad, or from public or private research centers.

L'archive ouverte pluridisciplinaire **HAL**, est destinée au dépôt et à la diffusion de documents scientifiques de niveau recherche, publiés ou non, émanant des établissements d'enseignement et de recherche français ou étrangers, des laboratoires publics ou privés.



# Fully decoupled time-marching schemes for incompressible fluid/thin-walled structure interaction

Miguel A. Fernández, Mikel Landajuela

**RESEARCH  
REPORT**

**N° 8425**

December 2013

Project-Team Reo





## Fully decoupled time-marching schemes for incompressible fluid/thin-walled structure interaction

Miguel A. Fernández <sup>\*†</sup>, Mikel Landajuela<sup>\*</sup>

Project-Team Reo

Research Report n° 8425 — December 2013 — 24 pages

**Abstract:** In this paper we introduce a class of fully decoupled time-marching schemes (velocity-pressure-displacement splitting) for the coupling of an incompressible fluid with a thin-walled viscoelastic structure. The time splitting combines a fractional-step time-marching in the fluid with a specific Robin-Neumann treatment of the interface coupling. A priori energy estimates guaranteeing unconditional stability are established for the variants without extrapolation and with first-order extrapolation. The accuracy and performance of the methods proposed are discussed in several numerical examples.

**Key-words:** fluid-structure interaction, incompressible fluid, Reissner-Mindlin shell, time-discretization, fractional-step method, loosely coupled scheme

---

This work was supported by the French National Research Agency (ANR) through the EXIFSI project (ANR-12-JS01-0004).

\* Inria, REO project-team, Rocquencourt - B.P. 105, F-78153 Le Chesnay cedex, France

† UPMC Université Paris VI, REO project-team, UMR 7958 LJLL, F-75005 Paris, France

**RESEARCH CENTRE  
PARIS – ROCQUENCOURT**

Domaine de Voluceau, - Rocquencourt  
B.P. 105 - 78153 Le Chesnay Cedex

# Schémas de couplage totalement découplés pour l'interaction d'un fluide incompressible et une structure mince

**Résumé :** Dans cet article, nous introduisons une classe de schémas entièrement découplés (vitesse-pression-déplacement) pour le couplage d'un fluide incompressible avec une structure viscoélastique mince. Les méthodes combinent une discrétisation à pas fractionnaire globale du système couplé avec un traitement spécifique Robin-Neumann du couplage à l'interface. Des estimations d'énergie a priori garantissent la stabilité inconditionnelle des variantes sans extrapolation et avec extrapolation d'ordre un. La précision et la robustesse des méthodes proposées sont illustrées dans plusieurs exemples numériques.

**Mots-clés :** interaction fluide-structure, fluide incompressible, modèle de coque Reissner-Mindlin, discrétisation en temps, méthode à pas fractionnaire, schéma de couplage faible

## 1 Introduction

Mathematical problems describing the coupling of a deformable thin-walled structure with an incompressible fluid flow appear in a wide variety of engineering fields: from the aeroelasticity of parachutes and sailing boats, to sloshing dynamics in tanks, heat exchanger tubes, and the biomechanics of air and blood flow (see, e.g., [36, 28, 11, 33, 25, 30]).

The numerical approximation of this type of problems is particularly sensitive to the way the interface coupling conditions (kinematic and kinetic continuity) are enforced at the discrete level. This is due to the fact that the interface coupling is very stiff. Explicit coupling (or *loosely coupled*) schemes, that only involve the solution of the fluid and of the structure once per time-step, are known to be unconditionally unstable for standard Dirichlet-Neumann strategies whenever the amount of added-mass in the system is large (see, e.g., [7, 20]). This explains the tremendous research effort devoted, over the last decade, to the design of robust methods based on alternative coupling paradigms (see, e.g., [12] for a recent review).

Fractional-step methods have played a major role in this attempt (see, e.g., [14, 34, 3, 1, 2, 23, 16, 13, 17, 5, 29]). In these approaches, added-mass free stability is achieved by combining a fractional-step time-marching in the fluid (see, e.g., [14, 34, 3, 1, 2]) or in the solid (see, e.g., [23, 13, 17, 5, 29]) with a specific explicit/implicit treatment of the interface conditions. The implicit part of the coupling guarantees stability while the explicit one reduces computational complexity.

The fluid pressure and the solid system are implicitly coupled in the semi-implicit schemes introduced in [14, 34, 3, 1, 2]. In the case of the coupling with a thin-walled structure, the semi-implicit schemes reported in [23, 5, 29] treat implicitly the whole solid hydrodynamic contributions –inertial and viscous effects– within the fluid, through a non-standard interface Robin condition. Full fluid-solid splitting (i.e., explicit coupling) is achieved with the explicit Robin-Neumann schemes introduced in [13, 17]. These methods only treat implicitly the solid inertia within the monolithic fluid time-stepping, which yields a standard interface Robin condition for the fluid. Optimal accuracy is achieved via extrapolation.

Though different degrees of fluid-solid splitting are obtained with the above coupling schemes, none of them enable the fully decoupled time-marching of the entire fluid-solid state, namely, fluid velocity, fluid pressure and solid displacement. In this work, we introduce a class of methods for the coupling of an incompressible fluid with a general thin-walled structure which (for the first time) achieve this purpose. Basically, the schemes combine the fluid-solid splitting paradigm of [13, 17] with a Chorin-Temam time-stepping in the fluid (see, e.g., [22, 9, 37]). The key ingredient of the methods lies in the specific fractional-step time discretization of the interface Robin consistency, which preserves the stability and accuracy of the fluid-solid splitting without compromising the velocity/pressure uncoupling of the fluid time-marching.

A priori energy estimates are derived for some of the variants, guaranteeing added-mass free stability. Interestingly, the velocity/pressure splitting in the fluid introduces additional perturbations of the kinematic coupling which require particular treatments. Another salient difference with respect to [13, 17] is the fact the stability analysis is performed in a wider framework, involving the coupling with *Reissner-Mindlin* shell models (see, e.g., [8, 4]) useful for much engineering applications.

Several numerical experiments, based on different linear and non-linear fluid-structure interaction examples, illustrate the accuracy and performance of the methods proposed.

The rest of the paper is organized as follows. In Section 2, we introduce the general fluid-structure coupled problem. Section 3 presents the fully decoupled schemes in a time semi-discrete framework. Section 4 is devoted to the derivation and analysis of the methods within a simplified setting. The numerical experiments are presented in Section 5. Finally, a summary of the

conclusions and some directions of further investigation are reported in Section 6.

Some preliminary results of this work have been announced, without proof, in [15].

## 2 Problem setting

In this section we present the non-linear coupled problem that describes the mechanical interaction between a viscous incompressible fluid and a thin-walled viscoelastic structure. The fluid is modeled by the incompressible Navier-Stokes equations in ALE (arbitrary Lagrangian-Eulerian) formulation (see, e.g. [19, 10]). The structure is described by a *Reissner-Mindlin* shell model (see, e.g., [8, 4]).

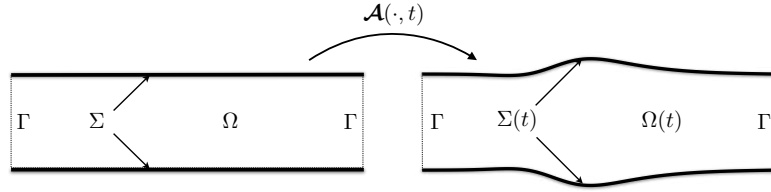


Figure 1: Geometrical description

We denote by  $\Omega \subset \mathbb{R}^3$  the reference configuration of the fluid domain and by  $\partial\Omega$  its boundary. The following partition  $\partial\Omega = \Gamma \cup \Sigma$  is considered, where  $\Sigma$  stands for the fluid-structure interface (see Figure 1). Since the structure is thin-walled, the interface  $\Sigma$  is itself the reference configuration of the shell mid-surface. The fluid domain motion is parametrized by the ALE map  $\mathcal{A} \stackrel{\text{def}}{=} \mathbf{I}_\Omega + \mathbf{d}^f$ , where  $\mathbf{d}^f : \Omega \times \mathbb{R}^+ \rightarrow \mathbb{R}^3$  stands for the fluid domain displacement. Hence, we have  $\Omega(t) = \mathcal{A}(\Omega, t)$ . The ALE time derivative operator is denoted by  $\partial_t|_{\mathcal{A}}$ . The symbol  $\mathbf{w} \stackrel{\text{def}}{=} \partial_t \mathcal{A} = \partial_t \mathbf{d}^f$  stands for the fluid domain velocity,  $\mathbf{F} \stackrel{\text{def}}{=} \nabla \mathcal{A}$  for the gradient of deformation and  $J \stackrel{\text{def}}{=} \det \mathbf{F}$  for the Jacobian. The exterior unit-vector normal to  $\partial\Omega$  is denoted by  $\mathbf{n}$ . For a given vector field  $\mathbf{v}$  defined on the surface  $\Sigma$ , the symbols  $\mathbf{v}_\perp \stackrel{\text{def}}{=} (\mathbf{v} \cdot \mathbf{n})\mathbf{n}$  and  $\mathbf{v}_\parallel \stackrel{\text{def}}{=} \mathbf{v} - \mathbf{v}_\perp$  denote, respectively, the normal and tangential components of  $\mathbf{v}$ .

The considered non-linear fluid-structure problem reads as follows: find the fluid domain displacement  $\mathbf{d}^f : \Omega \times \mathbb{R}^+ \rightarrow \mathbb{R}^3$ , the velocity  $\mathbf{u} : \Omega \times \mathbb{R}^+ \rightarrow \mathbb{R}^3$ , the pressure  $p : \Omega \times \mathbb{R}^+ \rightarrow \mathbb{R}$ , the solid mid-surface displacement  $\mathbf{d} : \Sigma \times \mathbb{R}^+ \rightarrow \mathbb{R}^3$  and the rotation vector  $\boldsymbol{\theta} : \Sigma \times \mathbb{R}^+ \rightarrow \mathbb{R}^3$ , satisfying the *Reissner-Mindlin* kinematical assumption  $\boldsymbol{\theta}_\perp = \mathbf{0}$ , such that

$$\left\{ \begin{array}{l} \mathbf{d}^f = \text{Ext}(\mathbf{d}|_\Sigma), \quad \mathbf{w} = \partial_t \mathbf{d}^f \quad \text{in } \Omega, \quad \Omega(t) = \mathcal{A}(\Omega, t), \\ \rho^f \partial_t|_{\mathcal{A}} \mathbf{u} + \rho^f (\mathbf{u} - \mathbf{w}) \cdot \nabla \mathbf{u} - \text{div} \boldsymbol{\sigma}(\mathbf{u}, p) = \mathbf{0} \quad \text{in } \Omega(t), \\ \text{div} \mathbf{u} = 0 \quad \text{in } \Omega(t), \\ \boldsymbol{\sigma}(\mathbf{u}, p) \mathbf{n} = -p \mathbf{n} \quad \text{on } \Gamma, \\ \mathbf{u} = \dot{\mathbf{d}} \quad \text{on } \Sigma, \\ \rho^s \epsilon \partial_t \dot{\mathbf{d}} + \mathbf{L}_d^e(\mathbf{d}, \boldsymbol{\theta}) + \mathbf{L}_d^v(\dot{\mathbf{d}}, \dot{\boldsymbol{\theta}}) = -J \boldsymbol{\sigma}(\mathbf{u}, p) (\mathbf{F})^{-T} \mathbf{n} \quad \text{on } \Sigma, \\ \mathbf{L}_\theta^e(\mathbf{d}, \boldsymbol{\theta}) + \mathbf{L}_\theta^v(\dot{\mathbf{d}}, \dot{\boldsymbol{\theta}}) = \mathbf{0} \quad \text{on } \Sigma, \\ \dot{\mathbf{d}} = \partial_t \mathbf{d}, \quad \dot{\boldsymbol{\theta}} = \partial_t \boldsymbol{\theta} \quad \text{on } \Sigma, \\ \mathbf{d} = \boldsymbol{\theta} = \mathbf{0} \quad \text{on } \partial\Sigma, \end{array} \right. \quad (1)$$

fulfilling the initial conditions  $\mathbf{u}(0) = \mathbf{u}_0$ ,  $\mathbf{d}(0) = \mathbf{d}_0$ ,  $\boldsymbol{\theta}(0) = \boldsymbol{\theta}_0$  and  $\dot{\mathbf{d}}(0) = \dot{\mathbf{d}}_0$ . The symbol  $\text{Ext}(\cdot)$  represents an arbitrary extension operator from the interface  $\Sigma$  into the fluid domain  $\Omega$  (e.g., an harmonic lifting operator). The constants  $\rho^f$  and  $\rho^s$  denote, respectively, the fluid and solid densities and  $\epsilon$  is the solid thickness. The fluid is assumed to be incompressible and Newtonian. The fluid Cauchy-stress tensor is hence given by the relation  $\boldsymbol{\sigma}(\mathbf{u}, p) \stackrel{\text{def}}{=} -p\mathbf{I} + 2\mu\boldsymbol{\varepsilon}(\mathbf{u})$ , with  $\boldsymbol{\varepsilon}(\mathbf{u}) \stackrel{\text{def}}{=} \frac{1}{2}(\nabla\mathbf{u} + \nabla\mathbf{u}^T)$  and where  $\mu$  stands for the fluid dynamic viscosity. A given pressure data  $p_\Gamma$  is prescribed on the fluid external boundary  $\Gamma$ . At last, the surface differential operators  $(\mathbf{L}_d^e, \mathbf{L}_\theta^e)$  and  $(\mathbf{L}_d^v, \mathbf{L}_\theta^v)$  describe the shell elastic and viscous contributions, respectively.

**Remark 1** *An useful expression for the viscous operator  $(\mathbf{L}_d^v, \mathbf{L}_\theta^v)$  is given by the relation:*

$$\mathbf{L}_d^v(\dot{\mathbf{d}}, \dot{\boldsymbol{\theta}}) = \alpha\rho^s\epsilon\dot{\mathbf{d}} + \beta D\mathbf{L}_d^e(\mathbf{d}, \boldsymbol{\theta})(\dot{\mathbf{d}}, \dot{\boldsymbol{\theta}}), \quad \mathbf{L}_\theta^v(\dot{\mathbf{d}}, \dot{\boldsymbol{\theta}}) = \beta D\mathbf{L}_\theta^e(\mathbf{d}, \boldsymbol{\theta})(\dot{\mathbf{d}}, \dot{\boldsymbol{\theta}}). \quad (3)$$

Here,  $\alpha, \beta > 0$  are given parameters and  $D\mathbf{L}_d^e(\mathbf{d}, \boldsymbol{\theta})$ ,  $D\mathbf{L}_\theta^e(\mathbf{d}, \boldsymbol{\theta})$  denote the Fréchet derivatives of  $\mathbf{L}_d^e, \mathbf{L}_\theta^e$  at  $(\mathbf{d}, \boldsymbol{\theta})$ . In the framework of artery wall modeling, the zeroth-order term describes the dissipative effects of external tissue (see [30]), while the differential term can be viewed as a generalization of the Kelvin-Voigt model (see, e.g., [26, 6, 38])

### 3 A class of fully decoupled schemes

In this section, we introduce time semi-discrete approximations of (1)-(2) which enable a fully decoupled time-marching of  $(\mathbf{d}^f, \mathbf{u}, p, \mathbf{d})$ . Basically, the idea consists in combining the thin-walled nature of the structure with a velocity/pressure splitting of the fluid problem based on the Chorin-Temam projection scheme. In what follows,  $\tau > 0$  denotes the time-step size,  $t_n \stackrel{\text{def}}{=} n\tau$ , for  $n \in \mathbb{N}$ , and  $\partial_\tau x^n \stackrel{\text{def}}{=} (x^n - x^{n-1})/\tau$  the first order backward difference in time. We will make use of the superscript  $*$  to indicate zeroth- (i.e., without), first-order or second-order extrapolation from the previous time-steps, namely,  $x^* = 0$  if  $r = 0$ ,  $x^* = x^{n-1}$  if  $r = 1$  and  $x^* = 2x^{n-1} - x^{n-2}$  if  $r = 2$ , where  $r$  denotes the extrapolation order. Using this notation, the proposed time semi-discrete approximations of (1)-(2) are reported in Algorithm 1. For the detailed derivation of the schemes, the reader is referred to Section 4.

A salient feature of Algorithm 1 is its eminently explicit nature. The fluid domain geometry update is treated explicitly in the first step while the three subsequent steps perform a fully decoupled sequential computation of  $\mathbf{u}^n$ ,  $p^n$  and  $\mathbf{d}^n$ . We will see in Section 4.2 below that, for a representative linear setting, all this level of explicitness does not compromise energy stability. In fact, the key ingredient for stability is the underlying implicit fluid-pressure/solid-inertia coupling involved in the projection sub-step (6).

Another important aspect of the scheme is its intrinsic partitioned (or modular) character, in the sense that the overall fluid problem (4)-(6) does not depend on the specific structure of the solid model, and viceversa. In particular, the solid sub-step (7) is simply an implicit first-order time-discretization of the shell equations (2)<sub>2-5</sub> with a known forcing term. Note also that the interface Robin conditions (5)<sub>3</sub> and (6)<sub>3</sub> are nothing but consistent relaxations of the kinematic compatibility (2)<sub>1</sub>. In this sense, it is worth recalling that for pressure-correction Chorin-Temam fractional-step methods, Dirichlet conditions on the velocity yield homogeneous Neumann conditions for the pressure (see, e.g., [21, 22]).

**Remark 2** *For  $r = 1$  or  $2$ , Algorithm 1 is a multi-step method, since initial data is required at steps  $1, \dots, 1+r-1$ . In what follows, this additional data is obtained by performing, respectively, one step of Algorithm 1 with  $r = 0$  and then one step with  $r = 1$ .*



and the rotation vector  $\boldsymbol{\theta} : \Sigma \times \mathbb{R}^+ \rightarrow \mathbb{R}^3$ , with  $\boldsymbol{\theta}_\perp = \mathbf{0}$ , such that

$$\begin{cases} \rho^f \partial_t \mathbf{u} - \mathbf{div} \boldsymbol{\sigma}(\mathbf{u}, p) = \mathbf{0} & \text{in } \Omega, \\ \mathbf{div} \mathbf{u} = 0 & \text{in } \Omega, \\ \boldsymbol{\sigma}(\mathbf{u}, p) \mathbf{n} = -p_\Gamma \mathbf{n} & \text{on } \Gamma, \end{cases} \quad (8)$$

$$\begin{cases} \mathbf{u} = \dot{\mathbf{d}} & \text{on } \Sigma, \\ \rho^s \epsilon \partial_t \dot{\mathbf{d}} + \mathbf{L}_d^e(\mathbf{d}, \boldsymbol{\theta}) + \mathbf{L}_d^v(\dot{\mathbf{d}}, \dot{\boldsymbol{\theta}}) = -\boldsymbol{\sigma}(\mathbf{u}, p) \mathbf{n} & \text{on } \Sigma, \\ \mathbf{L}_\theta^e(\mathbf{d}, \boldsymbol{\theta}) + \mathbf{L}_\theta^v(\dot{\mathbf{d}}, \dot{\boldsymbol{\theta}}) = \mathbf{0} & \text{on } \Sigma, \\ \dot{\mathbf{d}} = \partial_t \mathbf{d}, \quad \dot{\boldsymbol{\theta}} = \partial_t \boldsymbol{\theta} & \text{on } \Sigma, \\ \mathbf{d} = \boldsymbol{\theta} = \mathbf{0} & \text{on } \partial \Sigma, \end{cases} \quad (9)$$

satisfying the initial conditions  $\mathbf{u}(0) = \mathbf{u}_0$ ,  $\mathbf{d}(0) = \mathbf{d}_0$ ,  $\boldsymbol{\theta}(0) = \boldsymbol{\theta}_0$  and  $\dot{\mathbf{d}}(0) = \dot{\mathbf{d}}_0$ . In this section, the elastic and viscous solid operators,  $(\mathbf{L}_d^e, \mathbf{L}_\theta^e)$  and  $(\mathbf{L}_d^v, \mathbf{L}_\theta^v)$ , are supposed to be linear.

**Remark 3** Problem (8)-(9) retains all the added-mass effect numerical issues that appear in complex non-linear incompressible fluid-structure interaction problems. It is also worth noting that, unlike [13, 17, 15], the present simplified setting involves the coupling with a Reissner-Mindlin shell model.

#### 4.1 Time semi-discretization

This section is devoted to the time discretization of the coupled problem (8)-(9). The same considerations apply to the general non-linear problem (1)-(2). A salient feature of the coupled system (8)-(9) is its intrinsic Robin consistency on the interface, intimately related to the thin-walled nature of the structure. More specifically, from (9)<sub>1,2</sub> we infer that

$$\boldsymbol{\sigma}(\mathbf{u}, p) \mathbf{n} + \rho^s \epsilon \partial_t \mathbf{u} = -\mathbf{L}_d^e(\mathbf{d}, \boldsymbol{\theta}) - \mathbf{L}_d^v(\dot{\mathbf{d}}, \dot{\boldsymbol{\theta}}) \quad \text{on } \Sigma, \quad (10)$$

which can be viewed as a Robin-like boundary condition for the fluid (see also [31, 23, 13, 17]). This notion of interface Robin consistency has recently been used in the literature to avoid, without compromising optimal accuracy, the infamous unconditional instability issues of standard loosely coupled schemes (see [13, 17]). Basically, these methods split the time-marching of  $(\mathbf{u}, p)$  and  $\mathbf{d}$ . The schemes proposed in this work enable the fully decoupled sequential computation of the whole fluid-solid state:  $\mathbf{u}$ ,  $p$  and  $\mathbf{d}$ .

The solution procedures proposed in this paper build on the following three fundamental ingredients:

1. Fractional-step time-marching of the fluid via the standard Chorin-Temam projection scheme (see, e.g., [22, 9, 37]):

(a) Viscous-step:

$$\begin{cases} \rho^f \frac{\tilde{\mathbf{u}}^n - \mathbf{u}^{n-1}}{\tau} - 2\mu \mathbf{div} \boldsymbol{\varepsilon}(\tilde{\mathbf{u}}^n) = \mathbf{0} & \text{in } \Omega, \\ 2\mu \boldsymbol{\varepsilon}(\tilde{\mathbf{u}}^n) \mathbf{n} = \mathbf{0} & \text{on } \Gamma. \end{cases} \quad (11)$$

(b) Projection-step:

$$\begin{cases} \rho^f \frac{\mathbf{u}^n - \tilde{\mathbf{u}}^n}{\tau} + \nabla p^n = \mathbf{0} & \text{in } \Omega, \\ \mathbf{div} \mathbf{u}^n = 0 & \text{in } \Omega, \\ p^n = p_\Gamma & \text{on } \Gamma. \end{cases} \quad (12)$$

2. Explicit interface conditions for (11) and (12), based on a specific fractional-step time-marching of (10), which preserve the velocity/pressure splitting and treat implicitly the solid-inertia contributions.
3. Fluid stresses are transmitted to the solid by solving the standard shell problem:

$$\left\{ \begin{array}{ll} \rho^s \epsilon \partial_\tau \dot{\mathbf{d}}^n + \mathbf{L}_d^e(\mathbf{d}^n, \boldsymbol{\theta}^n) + \mathbf{L}_d^v(\dot{\mathbf{d}}^n, \dot{\boldsymbol{\theta}}^n) = -\boldsymbol{\sigma}(\tilde{\mathbf{u}}^n, p^n) \mathbf{n} & \text{on } \Sigma, \\ \mathbf{L}_\theta^e(\mathbf{d}^n, \boldsymbol{\theta}^n) + \mathbf{L}_\theta^v(\dot{\mathbf{d}}^n, \dot{\boldsymbol{\theta}}^n) = \mathbf{0} & \text{on } \Sigma, \\ \dot{\mathbf{d}} = \partial_\tau \mathbf{d}^n, \quad \dot{\boldsymbol{\theta}}^n = \partial_\tau \boldsymbol{\theta}^n & \text{on } \Sigma, \\ \mathbf{d}^n = \boldsymbol{\theta}^n = \mathbf{0} & \text{on } \partial\Sigma. \end{array} \right. \quad (13)$$

We now further elaborate on the second point. We first note that the projection-step (12) only contributes to the normal component of the fluid-stress, that is,  $-p = \boldsymbol{\sigma}(\mathbf{u}, p) \mathbf{n} \cdot \mathbf{n}$ . This is consistent with the fact that, in (12), only the normal component of the velocity has a well-defined trace on  $\Sigma$ . In terms of interface coupling, this indicates that the projection-step only contributes to the normal component of (10). Therefore, its tangential component has to be taken into account in the viscous-step (11). We thus propose the following two-stage time discretization of (10):

$$\left\{ \begin{array}{ll} 2\mu\boldsymbol{\varepsilon}(\tilde{\mathbf{u}}^n) \mathbf{n} + \frac{\rho^s \epsilon}{\tau} \tilde{\mathbf{u}}^n = \frac{\rho^s \epsilon}{\tau} \dot{\mathbf{d}}^{n-1} - \mathbf{L}_d^e(\mathbf{d}^*, \boldsymbol{\theta}^*)_{\parallel} - \mathbf{L}_d^v(\dot{\mathbf{d}}^*, \dot{\boldsymbol{\theta}}^*)_{\parallel} & \text{on } \Sigma, \\ -p^n + \frac{\rho^s \epsilon}{\tau} \mathbf{u}^n \cdot \mathbf{n} = \frac{\rho^s \epsilon}{\tau} \tilde{\mathbf{u}}^n \cdot \mathbf{n} - \mathbf{L}_d^e(\mathbf{d}^*, \boldsymbol{\theta}^*) \cdot \mathbf{n} - \mathbf{L}_d^v(\dot{\mathbf{d}}^*, \dot{\boldsymbol{\theta}}^*) \cdot \mathbf{n} & \text{on } \Sigma. \end{array} \right. \quad (14)$$

These interface relations preserve the original splitting of (11) and (12) and enable the interface fluid-solid splitting through the explicit treatment of the solid viscoelastic terms in (14). Besides, these extrapolations are performed to control the perturbation of the kinematic coupling, which dramatically affects accuracy in practice (see Section 5).

In summary, a three-stage splitting of the coupled problem (8)-(9) can be performed by solving (11) with (14)<sub>1</sub>, then (12) with (14)<sub>2</sub> and finally (13). The fully decoupled schemes proposed in this paper combine this approach with two additional refinements. First, in order to avoid the extrapolations of the solid viscoelastic terms in (14), we instead consider the following equivalent interface relations

$$\left\{ \begin{array}{ll} 2\mu\boldsymbol{\varepsilon}(\mathbf{u}^n) \mathbf{n} + \frac{\rho^s \epsilon}{\tau} \mathbf{u}^n = \frac{\rho^s \epsilon}{\tau} (\dot{\mathbf{d}}^{n-1} + \tau \partial_\tau \dot{\mathbf{d}}^*) + (2\mu\boldsymbol{\varepsilon}(\tilde{\mathbf{u}}^*) \mathbf{n})_{\parallel} & \text{on } \Sigma, \\ -p^n + \frac{\rho^s \epsilon}{\tau} \mathbf{u}^n \cdot \mathbf{n} = \frac{\rho^s \epsilon}{\tau} \tilde{\mathbf{u}}^n \cdot \mathbf{n} - p^* + \frac{\rho^s \epsilon}{\tau} (\dot{\mathbf{d}}^* - \tilde{\mathbf{u}}^*) \cdot \mathbf{n} & \text{on } \Sigma \end{array} \right. \quad (15)$$

for  $n \geq r + 1$ . To this purpose, we first note that from (13)<sub>1</sub> it follows that

$$-\mathbf{L}_d^e(\mathbf{d}^*, \boldsymbol{\theta}^*) - \mathbf{L}_d^v(\dot{\mathbf{d}}^*, \dot{\boldsymbol{\theta}}^*) = \rho^s \epsilon \partial_\tau \dot{\mathbf{d}}^* + \boldsymbol{\sigma}(\tilde{\mathbf{u}}^*, p^*) \mathbf{n} \quad (16)$$

for  $n \geq r + 1$ . The relation (15)<sub>1</sub> simply follows by inserting the tangential component of (16) into (14)<sub>1</sub>. Similarly, by combining (16) with (15)<sub>1</sub> we infer that

$$\begin{aligned} -\mathbf{L}_d^e(\mathbf{d}^*, \boldsymbol{\theta}^*) \cdot \mathbf{n} - \mathbf{L}_d^v(\dot{\mathbf{d}}^*, \dot{\boldsymbol{\theta}}^*) \cdot \mathbf{n} &= -p^* + \rho^s \epsilon \partial_\tau \dot{\mathbf{d}}^* \cdot \mathbf{n} - \frac{\rho^s \epsilon}{\tau} (\tilde{\mathbf{u}}^* - \dot{\mathbf{d}}^{*-1}) \cdot \mathbf{n} \\ &= -p^* + \frac{\rho^s \epsilon}{\tau} (\dot{\mathbf{d}}^* - \tilde{\mathbf{u}}^*) \cdot \mathbf{n}. \end{aligned}$$

By inserting this expression into (14)<sub>2</sub> we get (15)<sub>2</sub>. At last, instead of the Darcy-step (12), we consider the equivalent pressure-Poisson formulation complemented with the following interface Robin condition, derived from (15)<sub>2</sub>:

$$\frac{\tau}{\rho^f} \frac{\partial p^n}{\partial \mathbf{n}} = -(\mathbf{u}^n - \tilde{\mathbf{u}}^n) \cdot \mathbf{n} = \frac{\tau}{\rho^s \epsilon} (p^* - p^n) + (\tilde{\mathbf{u}}^* - \dot{\mathbf{d}}^*) \cdot \mathbf{n} \quad \text{on } \Sigma.$$

The proposed fully decoupled schemes for problem (8)-(9) are detailed in Algorithm 2.

---

**Algorithm 2** Fully decoupled schemes for (8)-(9)

---

For  $n \geq r + 1$ :

1. Fluid viscous sub-step: find  $\tilde{\mathbf{u}}^n : \Omega \rightarrow \mathbb{R}^d$  such that

$$\left\{ \begin{array}{ll} \rho^f \frac{\tilde{\mathbf{u}}^n - \mathbf{u}^{n-1}}{\tau} - 2\mu \mathbf{div} \boldsymbol{\varepsilon}(\tilde{\mathbf{u}}^n) = \mathbf{0} & \text{in } \Omega, \\ 2\mu \boldsymbol{\varepsilon}(\mathbf{u}^n) \mathbf{n} = \mathbf{0} & \text{on } \Gamma, \\ 2\mu \boldsymbol{\varepsilon}(\mathbf{u}^n) \mathbf{n} + \frac{\rho^s \epsilon}{\tau} \mathbf{u}^n = \frac{\rho^s \epsilon}{\tau} (\dot{\mathbf{d}}^{n-1} + \tau \partial_\tau \dot{\mathbf{d}}^*) + (2\mu \boldsymbol{\varepsilon}(\tilde{\mathbf{u}}^*) \mathbf{n})_{\parallel} & \text{on } \Sigma. \end{array} \right. \quad (17)$$

2. Fluid projection sub-step: find  $p^n : \Omega \rightarrow \mathbb{R}$  such that

$$\left\{ \begin{array}{ll} -\frac{\tau}{\rho^f} \Delta p^n = -\mathbf{div} \tilde{\mathbf{u}}^n & \text{in } \Omega, \\ p^n = p_\Gamma & \text{on } \Gamma, \\ \frac{\tau}{\rho^f} \frac{\partial p^n}{\partial \mathbf{n}} + \frac{\tau}{\rho^s \epsilon} p^n = \frac{\tau}{\rho^s \epsilon} p^* + (\tilde{\mathbf{u}}^* - \dot{\mathbf{d}}^*) \cdot \mathbf{n} & \text{on } \Sigma. \end{array} \right. \quad (18)$$

Thereafter set  $\mathbf{u}^n = \tilde{\mathbf{u}}^n - \frac{\tau}{\rho^f} \nabla p^n$ .

3. Solid sub-step: find  $\mathbf{d}^n : \Sigma \rightarrow \mathbb{R}^3$  and  $\boldsymbol{\theta}^n : \Sigma \rightarrow \mathbb{R}^3$  with  $\boldsymbol{\theta}_\perp^n = \mathbf{0}$  and such that

$$\left\{ \begin{array}{ll} \rho^s \epsilon \partial_\tau \dot{\mathbf{d}}^n + \mathbf{L}_d^e(\mathbf{d}^n, \boldsymbol{\theta}^n) + \mathbf{L}_d^v(\dot{\mathbf{d}}^n, \dot{\boldsymbol{\theta}}^n) = -\boldsymbol{\sigma}(\tilde{\mathbf{u}}^n, p^n) \mathbf{n} & \text{in } \Sigma, \\ \mathbf{L}_\theta^e(\mathbf{d}^n, \boldsymbol{\theta}^n) + \mathbf{L}_\theta^v(\dot{\mathbf{d}}^n, \dot{\boldsymbol{\theta}}^n) = \mathbf{0} & \text{on } \Sigma, \\ \dot{\mathbf{d}}^n = \partial_\tau \mathbf{d}^n, \quad \dot{\boldsymbol{\theta}}^n = \partial_\tau \boldsymbol{\theta}^n & \text{on } \Sigma, \\ \mathbf{d}^n = \boldsymbol{\theta}^n = \mathbf{0} & \text{on } \partial \Sigma. \end{array} \right. \quad (19)$$


---

## 4.2 Stability analysis

In this section, we provide an energy based estimate for Algorithm 2 with  $r = 0$  and  $r = 1$ .

### 4.2.1 Preliminaries

Let  $\omega$  be a given domain or surface in  $\mathbb{R}^3$ . In the succeeding text, the scalar product in  $L^2(\omega)$  is denoted by  $(\cdot, \cdot)_\omega$  and its norm by  $\|\cdot\|_\omega$ . Since the elastic and viscous solid surface operators,

$(\mathbf{L}_d^e, \mathbf{L}_\theta^e)$  and  $(\mathbf{L}_d^v, \mathbf{L}_\theta^v)$ , are supposed to be linear, they admit the following decomposition:

$$\begin{aligned} \mathbf{L}_d^e(\mathbf{d}, \boldsymbol{\theta}) &\stackrel{\text{def}}{=} \mathbf{A}_d^e \mathbf{d} + \mathbf{B}_d^e \boldsymbol{\theta}, & \mathbf{L}_d^v(\mathbf{d}, \boldsymbol{\theta}) &\stackrel{\text{def}}{=} \mathbf{A}_d^v \mathbf{d} + \mathbf{B}_d^v \boldsymbol{\theta}, \\ \mathbf{L}_\theta^e(\mathbf{d}, \boldsymbol{\theta}) &\stackrel{\text{def}}{=} \mathbf{B}_\theta^e \mathbf{d} + \mathbf{C}_\theta^e \boldsymbol{\theta}, & \mathbf{L}_\theta^v(\mathbf{d}, \boldsymbol{\theta}) &\stackrel{\text{def}}{=} \mathbf{B}_\theta^v \mathbf{d} + \mathbf{C}_\theta^v \boldsymbol{\theta}. \end{aligned}$$

We assume that the corresponding matrix operators

$$\mathbf{Q}^e \stackrel{\text{def}}{=} \begin{bmatrix} \mathbf{A}_d^e & \mathbf{B}_d^e \\ \mathbf{B}_\theta^e & \mathbf{C}_\theta^e \end{bmatrix}, \quad \mathbf{Q}^v \stackrel{\text{def}}{=} \begin{bmatrix} \mathbf{A}_d^v & \mathbf{B}_d^v \\ \mathbf{B}_\theta^v & \mathbf{C}_\theta^v \end{bmatrix},$$

are self-adjoint positive definite operators in  $[L^2(\Sigma)]^3 \times [L^2(\Sigma)]^3$ . The following notation will be used

$$\mathbf{y} \stackrel{\text{def}}{=} \begin{bmatrix} \mathbf{d} \\ \boldsymbol{\theta} \end{bmatrix}, \quad \dot{\mathbf{y}} \stackrel{\text{def}}{=} \begin{bmatrix} \dot{\mathbf{d}} \\ \dot{\boldsymbol{\theta}} \end{bmatrix}$$

and their corresponding elastic-energy and viscous-dissipation norms

$$\|\mathbf{y}\|_e \stackrel{\text{def}}{=} (\mathbf{Q}^e \mathbf{y}, \mathbf{y})_{\Sigma}^{\frac{1}{2}}, \quad \|\dot{\mathbf{y}}\|_v \stackrel{\text{def}}{=} (\mathbf{Q}^v \dot{\mathbf{y}}, \dot{\mathbf{y}})_{\Sigma}^{\frac{1}{2}}.$$

In order to ease the presentation, we will commit a slight abuse of notation by setting  $\mathbf{L}_d^e \mathbf{y} \stackrel{\text{def}}{=} \mathbf{L}_d^e(\mathbf{d}, \boldsymbol{\theta})$  and  $\mathbf{L}_d^v \dot{\mathbf{y}} \stackrel{\text{def}}{=} \mathbf{L}_d^v(\dot{\mathbf{d}}, \dot{\boldsymbol{\theta}})$ . The same applies to operators  $\mathbf{L}_\theta^e$  and  $\mathbf{L}_\theta^v$ . Finally, we define the time semi-discrete energy  $E^n$  and dissipation  $D^n$ , at time-step  $t_n$ , by

$$E^n \stackrel{\text{def}}{=} \frac{\rho^f}{2} \|\mathbf{u}^n\|_{\Omega}^2 + \frac{\rho^s \epsilon}{2} \|\mathbf{d}^n\|_{\Sigma}^2 + \frac{1}{2} \|\mathbf{y}^n\|_e^2, \quad D^n \stackrel{\text{def}}{=} 2\mu\tau \|\boldsymbol{\varepsilon}(\tilde{\mathbf{u}}^n)\|_{\Omega}^2 + \tau \|\dot{\mathbf{y}}^n\|_v^2.$$

#### 4.2.2 A priori energy estimate

The following result states the unconditional stability of the fully decoupled time-marching schemes provided by Algorithm 2 with  $r = 0$  or  $r = 1$ .

**Theorem 1** *Assume that the system is isolated, i.e.,  $p_{\Gamma} = 0$  (free system) and let the sequence  $\{(\tilde{\mathbf{u}}^n, \mathbf{u}^n, p^n, \mathbf{d}^n, \dot{\mathbf{d}}^n, \boldsymbol{\theta}^n, \dot{\boldsymbol{\theta}}^n)\}_{n \geq r+1}$  be given by Algorithm 2 with  $r = 0$  or  $r = 1$ . The following a priori energy estimate holds for  $n \geq r + 1$ :*

$$E^n + \sum_{m=r+1}^n D^m \leq E^0. \quad (20)$$

**Proof.** We first reformulate the second step of Algorithm 2 as the following equivalent Darcy-problem:

$$\left\{ \begin{array}{l} \rho^f \frac{\mathbf{u}^n - \tilde{\mathbf{u}}^n}{\tau} + \nabla p^n = \mathbf{0} \quad \text{in } \Omega, \\ \operatorname{div} \mathbf{u}^n = 0 \quad \text{in } \Omega, \\ p^n = p_{\Gamma} \quad \text{on } \Gamma, \\ p^n + \frac{\rho^s \epsilon}{\tau} \mathbf{u}^n \cdot \mathbf{n} = \frac{\rho^s \epsilon}{\tau} \tilde{\mathbf{u}}^n \cdot \mathbf{n} - p^* + \frac{\rho^s \epsilon}{\tau} (\dot{\mathbf{d}}^* - \tilde{\mathbf{u}}^*) \cdot \mathbf{n} \quad \text{on } \Sigma. \end{array} \right. \quad (21)$$

Note that, from (17)<sub>3</sub>, (19)<sub>1</sub> and (21)<sub>4</sub>, it follows that (14) holds for  $n \geq r + 1$ . Thus, by adding (14)<sub>1</sub> to (14)<sub>2</sub> multiplied by  $\mathbf{n}$ , we get

$$\frac{\rho^s \epsilon}{\tau} \left( (\tilde{\mathbf{u}}_{\parallel}^n + \mathbf{u}_{\perp}^n) - \dot{\mathbf{d}}^{n-1} \right) + \mathbf{L}_d^e \mathbf{y}^* + \mathbf{L}_d^v \dot{\mathbf{y}}^* = -\boldsymbol{\sigma}(\tilde{\mathbf{u}}^n, p^n) \mathbf{n} \quad \text{on } \Sigma,$$

which, after subtraction from (19)<sub>1</sub>, yields the following fundamental displacement-velocity correction reformulation of the solid step:

$$\frac{\rho^s \epsilon}{\tau} \left( \dot{\mathbf{d}}^n - (\tilde{\mathbf{u}}_{\parallel}^n + \mathbf{u}_{\perp}^n) \right) + \mathbf{L}_d^e(\mathbf{y}^n - \mathbf{y}^*) + \mathbf{L}_d^v(\dot{\mathbf{y}}^n - \dot{\mathbf{y}}^*) = \mathbf{0} \quad \text{on } \Sigma \quad (22)$$

for  $n \geq r + 1$ .

As a result, from (14)<sub>2</sub> and (22), we obtain the following perturbed kinematic constraints on the interface  $\Sigma$ :

$$\begin{cases} \mathbf{u}^n \cdot \mathbf{n} = \tilde{\mathbf{u}}^n \cdot \mathbf{n} + \frac{\tau}{\rho^s \epsilon} (p^n - \mathbf{L}_d^e \mathbf{y}^* \cdot \mathbf{n} - \mathbf{L}_d^v \dot{\mathbf{y}}^* \cdot \mathbf{n}), \\ \tilde{\mathbf{u}}^n = \dot{\mathbf{d}}^n + \frac{\tau}{\rho^s \epsilon} (\mathbf{L}_d^e(\mathbf{y}^n - \mathbf{y}^*) + \mathbf{L}_d^v(\dot{\mathbf{y}}^n - \dot{\mathbf{y}}^*)) \\ - \frac{\tau}{\rho^s \epsilon} (p^n \mathbf{n} - (\mathbf{L}_d^e \mathbf{y}^*)_{\perp} - (\mathbf{L}_d^v \dot{\mathbf{y}}^*)_{\perp}) \end{cases} \quad (23)$$

for  $n \geq r + 1$ .

We now proceed by taking the scalar product of (17)<sub>1</sub> and (21)<sub>1</sub> with  $\tilde{\mathbf{u}}^n$  and  $\mathbf{u}^n$ , respectively. Hence, after integration by parts over  $\Omega$  and summation of the resulting expressions, this yields

$$\frac{\rho^f}{2\tau} (\|\mathbf{u}^n\|_{\Omega}^2 - \|\mathbf{u}^{n-1}\|_{\Omega}^2) + 2\mu \|\varepsilon(\tilde{\mathbf{u}}^n)\|_{\Omega}^2 - (2\mu \varepsilon(\tilde{\mathbf{u}}^n) \mathbf{n}, \tilde{\mathbf{u}}^n)_{\Sigma} + (p^n, \mathbf{u}^n \cdot \mathbf{n})_{\Sigma} \leq 0.$$

By inserting (23)<sub>1</sub> into the last term, we have

$$\begin{aligned} \frac{\rho^f}{2\tau} (\|\mathbf{u}^n\|_{\Omega}^2 - \|\mathbf{u}^{n-1}\|_{\Omega}^2) + 2\mu \|\varepsilon(\tilde{\mathbf{u}}^n)\|_{\Omega}^2 - (\boldsymbol{\sigma}(\tilde{\mathbf{u}}^n, p^n) \mathbf{n}, \tilde{\mathbf{u}}^n)_{\Sigma} \\ + \frac{\tau}{\rho^s \epsilon} (p^n \mathbf{n}, p^n \mathbf{n} - (\mathbf{L}_d^e \mathbf{y}^*)_{\perp} - (\mathbf{L}_d^v \dot{\mathbf{y}}^*)_{\perp})_{\Sigma} \leq 0. \end{aligned} \quad (24)$$

On the other hand, owing to (19)<sub>1</sub> and (23)<sub>2</sub>, we infer that

$$\begin{aligned} -(\boldsymbol{\sigma}(\tilde{\mathbf{u}}^n, p^n) \mathbf{n}, \tilde{\mathbf{u}}^n)_{\Sigma} &= \frac{\rho^s \epsilon}{2\tau} \left( \|\dot{\mathbf{d}}^n\|_{\Sigma}^2 - \|\dot{\mathbf{d}}^{n-1}\|_{\Sigma}^2 + \|\dot{\mathbf{d}}^n - \dot{\mathbf{d}}^{n-1}\|_{\Sigma}^2 \right) \\ &+ \underbrace{\left( \mathbf{L}_d^e \mathbf{y}^n + \mathbf{L}_d^v \dot{\mathbf{y}}^n, \dot{\mathbf{d}}^n \right)_{\Sigma}}_{T_0} \\ &+ \underbrace{\frac{\tau}{2\rho^s \epsilon} \left( \|\mathbf{L}_d^e \mathbf{y}^n + \mathbf{L}_d^v \dot{\mathbf{y}}^n\|_{\Sigma}^2 - \|\mathbf{L}_d^e \mathbf{y}^* + \mathbf{L}_d^v \dot{\mathbf{y}}^*\|_{\Sigma}^2 + \|\mathbf{L}_d^e(\mathbf{y}^n - \mathbf{y}^*) + \mathbf{L}_d^v(\dot{\mathbf{y}}^n - \dot{\mathbf{y}}^*)\|_{\Sigma}^2 \right)}_{T_1} \\ &+ \underbrace{\left( \dot{\mathbf{d}}^n - \dot{\mathbf{d}}^{n-1}, \mathbf{L}_d^e(\mathbf{y}^n - \mathbf{y}^*) + \mathbf{L}_d^v(\dot{\mathbf{y}}^n - \dot{\mathbf{y}}^*) \right)_{\Sigma}}_{T_2} \\ &- \underbrace{\left( \dot{\mathbf{d}}^n - \dot{\mathbf{d}}^{n-1}, p^n \mathbf{n} - (\mathbf{L}_d^e \mathbf{y}^*)_{\perp} - (\mathbf{L}_d^v \dot{\mathbf{y}}^*)_{\perp} \right)_{\Sigma}}_{T_3} \\ &- \frac{\tau}{\rho^s \epsilon} \left( \mathbf{L}_d^e \mathbf{y}^n + \mathbf{L}_d^v \dot{\mathbf{y}}^n, p^n \mathbf{n} - (\mathbf{L}_d^e \mathbf{y}^*)_{\perp} - (\mathbf{L}_d^v \dot{\mathbf{y}}^*)_{\perp} \right)_{\Sigma}. \end{aligned} \quad (25)$$

Note that, thanks to (19)<sub>2</sub>, for the term  $T_0$  we have

$$\begin{aligned} T_0 &= \left( \mathbf{L}_d^e \mathbf{y}^n + \mathbf{L}_d^v \dot{\mathbf{y}}^n, \dot{\mathbf{d}}^n \right)_\Sigma + \left( \mathbf{L}_\theta^e \mathbf{y}^n + \mathbf{L}_\theta^v \dot{\mathbf{y}}^n, \dot{\boldsymbol{\theta}}^n \right)_\Sigma \\ &= (\mathbf{Q}^e \dot{\mathbf{y}}^n, \mathbf{y}^n)_\Sigma + (\mathbf{Q}^v \dot{\mathbf{y}}^n, \dot{\mathbf{y}}^n)_\Sigma \\ &= \frac{1}{2\tau} \left( \|\mathbf{y}^n\|_e^2 - \|\mathbf{y}^{n-1}\|_e^2 + \|\mathbf{y}^n - \mathbf{y}^{n-1}\|_e^2 \right) + \|\dot{\mathbf{y}}^n\|_v^2. \end{aligned} \quad (26)$$

Hence, by inserting (26) into (25) and the resulting expression into (24), we get the following energy inequality

$$\begin{aligned} &\frac{\rho^f}{2\tau} \left( \|\mathbf{u}^n\|_\Omega^2 - \|\mathbf{u}^{n-1}\|_\Omega^2 \right) + 2\mu \|\boldsymbol{\varepsilon}(\tilde{\mathbf{u}}^n)\|_\Omega^2 + \frac{\rho^s \epsilon}{2\tau} \left( \|\dot{\mathbf{d}}^n\|_\Sigma^2 - \|\dot{\mathbf{d}}^{n-1}\|_\Sigma^2 + \|\dot{\mathbf{d}}^n - \dot{\mathbf{d}}^{n-1}\|_\Sigma^2 \right) \\ &\quad + \frac{1}{2\tau} \left( \|\mathbf{y}^n\|_e^2 - \|\mathbf{y}^{n-1}\|_e^2 + \|\mathbf{y}^n - \mathbf{y}^{n-1}\|_e^2 \right) + \|\dot{\mathbf{y}}^n\|_v^2 + T_1 + T_2 + T_3 \\ &\quad + \underbrace{\frac{\tau}{\rho^s \epsilon} \left( p^n \mathbf{n} - \mathbf{L}_d^e \mathbf{y}^n - \mathbf{L}_d^v \dot{\mathbf{y}}^n, p^n \mathbf{n} - (\mathbf{L}_d^e \mathbf{y}^*)_\perp - (\mathbf{L}_d^v \dot{\mathbf{y}}^*)_\perp \right)_\Sigma}_{T_4} \leq 0 \end{aligned} \quad (27)$$

for  $n \geq r + 1$ .

We proceed by treating each case of extrapolation,  $r = 0$  or  $r = 1$ , separately.

Algorithm 2 with  $r = 0$ . We have

$$T_2 + T_3 \geq -\frac{\rho^s \epsilon}{2\tau} \|\dot{\mathbf{d}}^n - \dot{\mathbf{d}}^{n-1}\|_\Sigma^2 - \frac{\tau}{2\rho^s \epsilon} \|\mathbf{L}_d^e \mathbf{y}^n + \mathbf{L}_d^v \dot{\mathbf{y}}^n - p^n \mathbf{n}\|_\Sigma^2$$

and

$$T_1 + T_4 = \frac{\tau}{2\rho^s \epsilon} \|p^n\|_\Sigma^2 + \frac{\tau}{2\rho^s \epsilon} \|\mathbf{L}_d^e \mathbf{y}^n + \mathbf{L}_d^v \dot{\mathbf{y}}^n - p^n \mathbf{n}\|_\Sigma^2 + \frac{\tau}{2\rho^s \epsilon} \|\mathbf{L}_d^e \mathbf{y}^n + \mathbf{L}_d^v \dot{\mathbf{y}}^n\|_\Sigma^2.$$

Therefore,

$$\sum_{i=1}^4 T_i \geq -\frac{\rho^s \epsilon}{2\tau} \|\dot{\mathbf{d}}^n - \dot{\mathbf{d}}^{n-1}\|_\Sigma^2 + \frac{\tau}{2\rho^s \epsilon} \|p^n\|_\Sigma^2 + \frac{\tau}{2\rho^s \epsilon} \|\mathbf{L}_d^e \mathbf{y}^n + \mathbf{L}_d^v \dot{\mathbf{y}}^n\|_\Sigma^2. \quad (28)$$

The estimate (20) then follows by inserting this expression into (27), multiplication by  $\tau$  and summation over  $m = 1, \dots, n$ .

Algorithm 2 with  $r = 1$ . From (19)<sub>2</sub>, we have

$$\begin{aligned} T_2 &= \tau^2 \left( \partial_\tau \dot{\mathbf{d}}^n, \mathbf{L}_d^e \dot{\mathbf{y}}^n + \mathbf{L}_d^v (\partial_\tau \dot{\mathbf{y}}^n) \right)_\Sigma + \tau^2 \left( \partial_\tau \dot{\boldsymbol{\theta}}^n, \mathbf{L}_\theta^e \dot{\mathbf{y}}^n + \mathbf{L}_\theta^v (\partial_\tau \dot{\mathbf{y}}^n) \right)_\Sigma \\ &= \tau^2 (\mathbf{Q}^e \dot{\mathbf{y}}^n, \partial_\tau \dot{\mathbf{y}}^n)_\Sigma + \tau^2 (\mathbf{Q}^v \partial_\tau \dot{\mathbf{y}}^n, \partial_\tau \dot{\mathbf{y}}^n)_\Sigma \\ &= \frac{\tau}{2} \left( \|\dot{\mathbf{y}}^n\|_e^2 - \|\dot{\mathbf{y}}^{n-1}\|_e^2 + \|\dot{\mathbf{y}}^n - \dot{\mathbf{y}}^{n-1}\|_e^2 \right) + \tau^2 \|\partial_\tau \dot{\mathbf{y}}^n\|_v^2 \end{aligned}$$

for  $n \geq 2$ . For the third term, we get

$$T_3 \geq -\frac{\rho^s \epsilon}{2\tau} \|\dot{\mathbf{d}}^n - \dot{\mathbf{d}}^{n-1}\|_\Sigma^2 - \frac{\tau}{2\rho^s \epsilon} \left\| (\mathbf{L}_d^e \dot{\mathbf{y}}^{n-1})_\perp + (\mathbf{L}_d^v \dot{\mathbf{y}}^{n-1})_\perp - p^n \mathbf{n} \right\|_\Sigma^2.$$

At last, the fourth term is estimated as follows

$$\begin{aligned}
T_4 &= \frac{\tau}{\rho^s \epsilon} (p^n \mathbf{n} - \mathbf{L}_d^e \mathbf{y}^n - \mathbf{L}_d^v \dot{\mathbf{y}}^n, p^n \mathbf{n} - (\mathbf{L}_d^e \mathbf{y}^{n-1})_\perp - (\mathbf{L}_d^v \dot{\mathbf{y}}^{n-1})_\perp)_\Sigma \\
&= \frac{\tau}{\rho^s \epsilon} (p^n \mathbf{n} - (\mathbf{L}_d^e \mathbf{y}^n)_\perp - (\mathbf{L}_d^v \dot{\mathbf{y}}^n)_\perp, p^n \mathbf{n} - (\mathbf{L}_d^e \mathbf{y}^{n-1})_\perp - (\mathbf{L}_d^v \dot{\mathbf{y}}^{n-1})_\perp)_\Sigma \\
&= \frac{\tau}{\rho^s \epsilon} \|p^n \mathbf{n} - (\mathbf{L}_d^e \mathbf{y}^{n-1})_\perp - (\mathbf{L}_d^v \dot{\mathbf{y}}^{n-1})_\perp\|_\Sigma^2 \\
&\quad - \frac{\tau}{\rho^s \epsilon} ((\mathbf{L}_d^e (\mathbf{y}^n - \mathbf{y}^{n-1}))_\perp + (\mathbf{L}_d^v (\dot{\mathbf{y}}^n - \dot{\mathbf{y}}^{n-1}))_\perp, p^n \mathbf{n} - (\mathbf{L}_d^e \mathbf{y}^{n-1})_\perp - (\mathbf{L}_d^v \dot{\mathbf{y}}^{n-1})_\perp)_\Sigma \\
&\geq \frac{\tau}{2\rho^s \epsilon} \|p^n \mathbf{n} - (\mathbf{L}_d^e \mathbf{y}^{n-1})_\perp - (\mathbf{L}_d^v \dot{\mathbf{y}}^{n-1})_\perp\|_\Sigma^2 \\
&\quad - \frac{\tau}{2\rho^s \epsilon} \|(\mathbf{L}_d^e (\mathbf{y}^n - \mathbf{y}^{n-1}))_\perp + (\mathbf{L}_d^v (\dot{\mathbf{y}}^n - \dot{\mathbf{y}}^{n-1}))_\perp\|_\Sigma^2.
\end{aligned}$$

Therefore, by collecting the above estimations, we get

$$\begin{aligned}
\sum_{i=1}^4 T_i &\geq -\frac{\rho^s \epsilon}{2\tau} \|\mathbf{d}^n - \mathbf{d}^{n-1}\|_\Sigma^2 + \frac{\tau}{2} (\|\dot{\mathbf{y}}^n\|_e^2 - \|\dot{\mathbf{y}}^{n-1}\|_e^2 + \|\dot{\mathbf{y}}^n - \dot{\mathbf{y}}^{n-1}\|_e^2) \\
&\quad + \tau^2 \|\partial_\tau \dot{\mathbf{y}}^n\|_v^2 + \frac{\tau}{2\rho^s \epsilon} (\|\mathbf{L}_d^e \mathbf{y}^n + \mathbf{L}_d^v \dot{\mathbf{y}}^n\|_\Sigma^2 - \|\mathbf{L}_d^e \mathbf{y}^{n-1} + \mathbf{L}_d^v \dot{\mathbf{y}}^{n-1}\|_\Sigma^2) \\
&\quad + \frac{\tau}{2\rho^s \epsilon} \|(\mathbf{L}_d^e (\mathbf{y}^n - \mathbf{y}^{n-1}))_\parallel + (\mathbf{L}_d^v (\dot{\mathbf{y}}^n - \dot{\mathbf{y}}^{n-1}))_\parallel\|_\Sigma^2.
\end{aligned}$$

Inserting this expression into (27), then multiplying by  $\tau$  and summing over  $m = 2, \dots, n$ , yields the estimate

$$E^n + \sum_{m=2}^n D^m \leq E^1 + \frac{\tau}{2} \|\mathbf{y}^1 - \mathbf{y}^0\|_e^2 + \frac{\tau^2}{2\rho^s \epsilon} \|\mathbf{L}_d^e \mathbf{y}^1 + \mathbf{L}_d^v \dot{\mathbf{y}}^1\|_\Sigma^2. \quad (29)$$

Owing to the initialization procedure (see Remark 2),  $\mathbf{y}^1$  and  $\dot{\mathbf{y}}^1$  are obtained from the scheme with  $r = 0$ . Hence, the right-hand side of (29) can be bounded from (20), with  $r = 0$ , and the numerical dissipation provided by (26) and (28) for  $n = 1$ . This completes the proof.  $\square$

**Remark 4** *The stability of Algorithm 2 with second-order extrapolation,  $r = 2$ , is not covered by the previous analysis. In fact, numerical evidence indicate that this scheme is stable under CFL-like conditions, whose derivation requires the analysis in a formulation including discretization in space. Preliminary investigations in this directions point out that the arguments used in the proof below can not be straightforwardly adapted to this fully discrete setting.*

## 5 Numerical experiments

In this section we illustrate the accuracy and performance of the proposed fully decoupled schemes in several numerical examples from the literature. Section 5.1 focuses on the linear model problem (8)-(9) in a simple two-dimensional geometry. Results based on the nonlinear case (1)-(2) and more complex geometries are presented in the succeeding Sections 5.2-5.4.

### 5.1 Convergence study in a two-dimensional test-case

The first example simulates the propagation of a pressure-wave within an elastic tube in two-dimensions. Basically, we couple the Stokes system (8) with a viscoelastic string model, i.e., in

(9) we take  $\mathbf{L}_\theta^e(\mathbf{d}, \theta) = \mathbf{0}$ ,  $\mathbf{L}_\theta^v(\dot{\mathbf{d}}, \dot{\theta}) = \mathbf{0}$ ,

$$\mathbf{d} = \begin{pmatrix} 0 \\ \mathbf{d}_y \end{pmatrix}, \quad \mathbf{L}_d^e(\mathbf{d}, \theta) = \begin{pmatrix} 0 \\ -\lambda_1 \partial_{xx} \mathbf{d}_y + \lambda_0 \mathbf{d}_y \end{pmatrix}, \quad \mathbf{L}_d^v(\dot{\mathbf{d}}, \dot{\theta}) = \begin{pmatrix} 0 \\ \alpha \rho^s \epsilon \dot{\mathbf{d}}_y - \beta \lambda_1 \partial_{xx} \dot{\mathbf{d}}_y \end{pmatrix}$$

with  $\lambda_1 \stackrel{\text{def}}{=} \frac{E\epsilon}{2(1+\nu)}$  and  $\lambda_0 \stackrel{\text{def}}{=} \frac{E\epsilon}{R^2(1-\nu^2)}$ , where  $E$  and  $\nu$ , respectively, denote the Young modulus and the Poisson ratio of the solid. Note that in this case the tangential contributions in (17)<sub>3</sub> (or (14)<sub>1</sub>) disappear (see [15]).

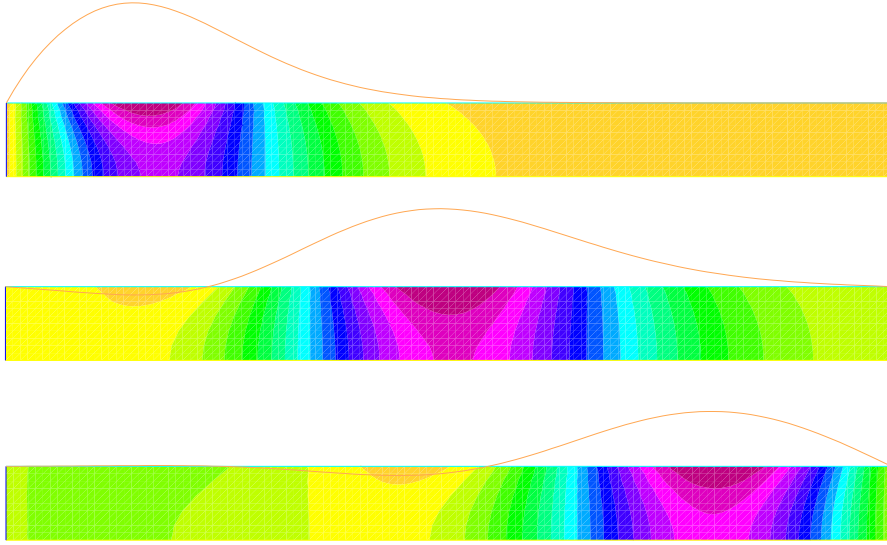


Figure 2: Snapshots of the fluid pressure and solid displacement at the time instants  $t = 0.005, 0.01, 0.015$  (from top to bottom). Algorithm 2 with first-order extrapolation,  $\tau = 10^{-4}$  and  $h = 0.05$ .

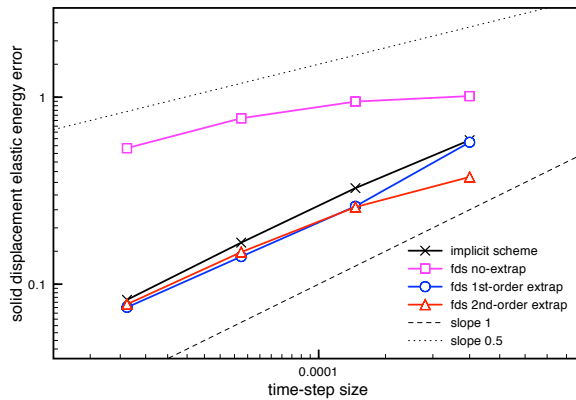


Figure 3: Time-convergence history of the displacement at  $t = 0.015$ , with  $h = \mathcal{O}(\tau)$ .

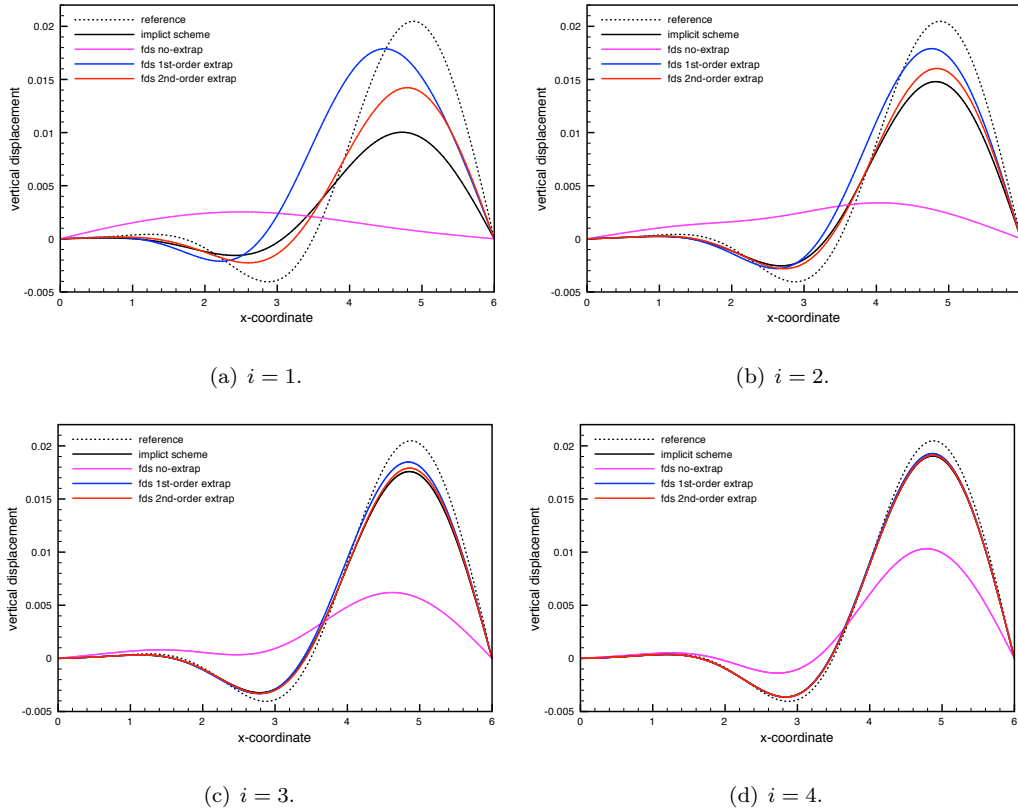


Figure 4: Comparison of the solid displacements at  $t = 0.015$  for different levels of  $(\tau, h)$ -refinement.

For the fluid we take  $\rho^f = 1.0$  and  $\mu = 0.035$ , and for the solid  $\rho^s = 1.1$ ,  $\epsilon = 0.1$ ,  $E = 0.75 \times 10^6$ ,  $\nu = 0.5$ ,  $\alpha = 1$  and  $\beta = 10^{-3}$ . All units are expressed in the CGS system. The fluid domain is given by  $\Omega = [0, L] \times [0, R]$  and the fluid-solid interface by  $\Sigma = [0, L] \times \{R\}$ , with  $L = 6$  and  $R = 0.5$ . At  $t = 0$  the whole system is at rest. A sinusoidal pressure-wave (with maximum  $2 \cdot 10^4$ ) is prescribed on the inlet boundary  $x = 0$  during  $5 \cdot 10^{-3}$  time instants. Zero pressure is imposed at  $x = 6$  and a slip condition is enforced on the lower boundary  $y = 0$ . For the solid we set  $\mathbf{d}_y = 0$  at  $x = 0, L$ . The spatial discretization of the fluid and of the structure is based on piece-wise affine continuous finite elements. The numerical tests have been carried out with FreeFem++ [24].

We first consider Algorithm 2 with  $r = 1$ ,  $\tau = 10^{-4}$  and  $h = 0.05$ . Figure 2 presents the snapshots of the pressure field and the solid displacement (amplified by a factor 5) at the time instants  $t = 0.005, 0.01$  and  $0.015$ . The scheme is able to reproduce a stable pressure-wave propagation. In order to assess the overall convergence rate of Algorithm 2, we have uniformly refined in time and in space under a hyperbolic-CFL condition ( $\tau = \mathcal{O}(h)$ ):  $(\tau, h) = \{5 \cdot 10^{-4}/2^i, 10^{-1}/2^i\}_{i=1}^4$ .

Figure 3 shows the relative elastic energy-norm error of the solid displacement, at time  $t = 0.015$ , obtained with Algorithm 2 and the different extrapolations ( $r = 0, 1, 2$ ). For comparison purposes the errors obtained with a fully implicit first-order scheme are also displayed. The reference solution has been computed with the implicit scheme and high space-time resolution:

$h = 3.125 \times 10^{-3}$  and  $\tau = 10^{-6}$ . The results of Figure 3 indicate that the proposed fully decoupled schemes with  $r = 1$  or  $r = 2$  are able to retrieve the optimal first-order convergence rate  $\mathcal{O}(\tau)$  of the implicit scheme. Conversely, a sub-optimal overall rate  $\mathcal{O}(\tau^{\frac{1}{2}})$  is observed for  $r = 0$ . The different accuracy of the schemes is also evidenced in Figure 4, which shows the displacements, at  $t = 0.015$ , obtained for different levels of space-time refinement. Similar accuracy, in terms of  $r$ , was observed in [13, 17] for the explicit Robin-Neumann schemes introduced therein.

## 5.2 Pressure wave propagation in a straight tube

The second numerical test is basically a three-dimensional non-linear version of the previous example (see, e.g., [19]). The physical system is described by the non-linear coupled problem (1)-(2), with a Saint Venant-Kirchhoff constitutive law for the solid.

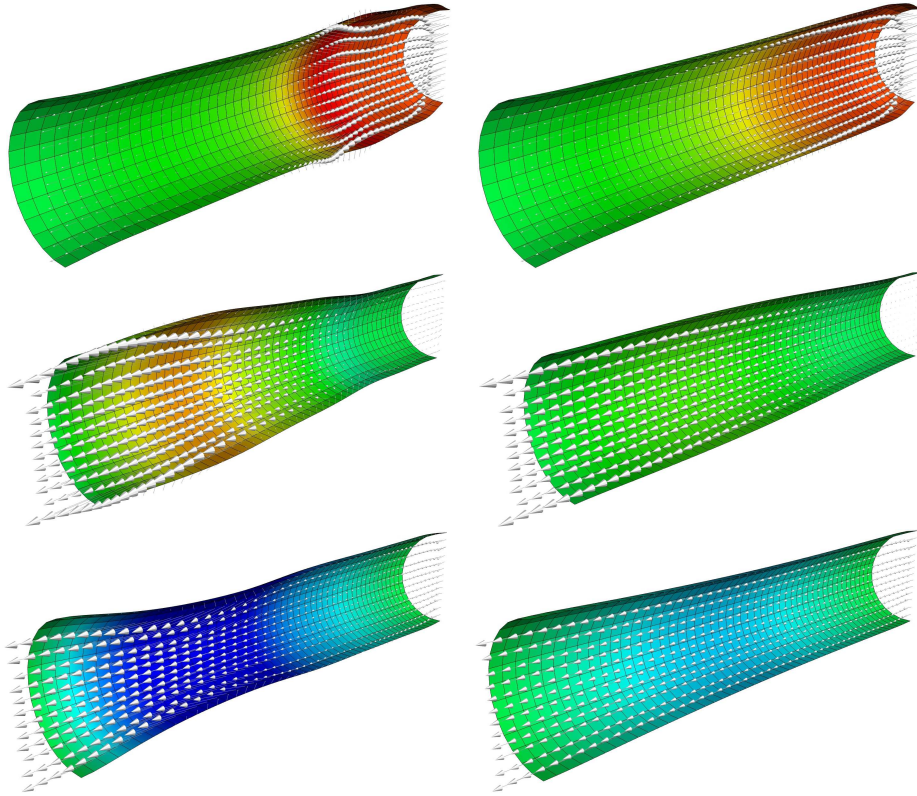


Figure 5: Snapshots of the velocity field and fluid interface pressure at  $t = 0.005, 0.01, 0.015$  (from top to bottom). Algorithm 1 with  $r = 1$  and  $\tau = 10^{-4}$ . Left: without solid damping ( $\alpha = \beta = 0$ ). Right: with solid damping ( $\alpha = 1, \beta = 10^{-3}$ ).

The fluid domain is a cylinder of radius  $R = 0.5$  and length  $L = 5$ . All the units are expressed in the CGS system. The physical parameters of the fluid are  $\rho^f = 1.0$  and  $\mu = 0.035$ . For the structure we take  $\rho^s = 1.2$ ,  $\epsilon = 0.1$ ,  $E = 3 \times 10^6$  and  $\nu = 0.5$ . Damping effects in the solid are modeled through the expression (3) with  $\alpha = 1$ ,  $\beta = 10^{-3}$ . A constant pressure of  $1.3332 \times 10^4$  is imposed on the inlet boundary during  $5 \cdot 10^{-3}$  time instants, thereafter this value is set to zero. An homogeneous natural boundary condition is prescribed on the outlet boundary. The whole fluid-solid system is initially at rest.

Both the velocity and the pressure are discretized in space using  $\mathbb{Q}_1$  finite elements. A streamline-upwind/Petrov-Galerkin (SUPG) stabilization is applied to the viscous sub-step (5) of Algorithm 1. The shell equation is discretized in space by quadrilateral MITC4 elements (see [8, Section 8.2.1]). The time-step length is set to  $\tau = 10^{-4}$ .

We first consider Algorithm 1 with the first-order extrapolation ( $r = 1$ ). Figure 5 shows the fluid velocity field and the solid deformation (amplified by a factor 10) obtained at the time instants  $t = 0.005$ ,  $0.01$  and  $0.015$ . Both the undamped (left) and damped (right) solid cases are displayed. The well-known propagating pressure-wave is observed in both situations, being clearly deflated when damping effects are incorporated in the solid model.

The interface mid-point displacement magnitudes obtained with Algorithm 1 (in its three variants  $r = 0, 1, 2$ ) and with a first-order implicit scheme are displayed in Figure 6. Similar observations than in Section 5.1 can be inferred from these results: the accuracy of the implicit scheme is retrieved by Algorithm 1 with  $r = 1$  or  $r = 2$ , while for  $r = 0$  the fully decoupled scheme yields a highly inaccurate numerical approximation.

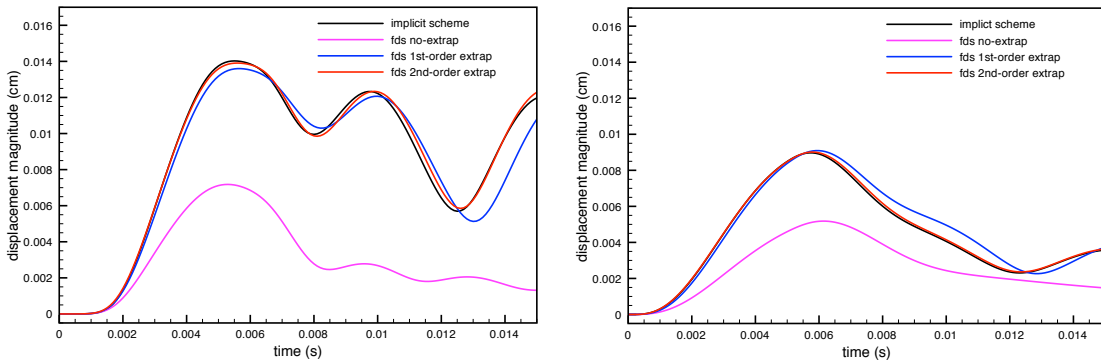


Figure 6: Comparison of Algorithm 1 and the implicit scheme: interface mid-point displacement magnitude *vs.* time. Left: without solid damping ( $\alpha = \beta = 0$ ). Right: with solid damping ( $\alpha = 1$ ,  $\beta = 10^{-3}$ ).

### 5.3 Blood flow in an abdominal aortic aneurysm

In this example we simulate the blood flow within an in-vitro abdominal aortic aneurysm geometry (see, e.g., [35, 1, 17]). The physical system is here described by the coupled problem (1)-(2), with a Saint Venant-Kirchhoff constitutive relation for the aneurysm wall. The fluid-solid interface has a length of 22.95 and a uniform thickness of  $\epsilon = 0.17$ . All units are expressed in the CGS system. We take  $\rho^f = 1.0$  and  $\mu = 0.035$  in the fluid and  $\rho^s = 1.2$ ,  $E = 3 \times 10^6$ ,  $\nu = 0.5$ ,  $\alpha = 1$  and  $\beta = 10^{-3}$  in the solid. The fluid and structure are initially at rest. On the inlet boundary, we impose a physiological flow rate waveform (see Figure 7) measured at the level of the infrarenal aorta (see [32]). In order to obtain physiological pressure levels within the aneurysm, a resistance boundary condition is enforced on the outlet boundary. The value of the resistance is set to  $R_{\text{out}} = 600$ .

We consider Algorithm 1 with the same spatial discretization than in the previous example. The simulations are performed over 2000 time steps of size  $\tau = 4.2 \times 10^{-4}$  seconds (i.e., one cardiac cycle). We first consider Algorithm 1 with  $r = 1$ . In Figure 7 we display the obtained velocity field and the solid deformation at  $t = 0.042$ ,  $0.168$ ,  $0.294$ ,  $0.42$  (half the geometry).

The accuracy of all the fully decoupled schemes is illustrated in Figure 8, where the different

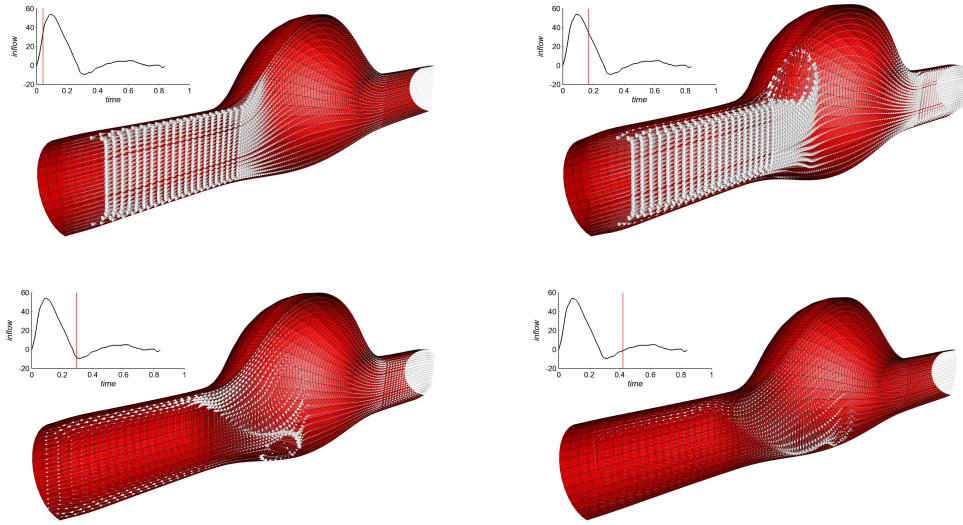


Figure 7: Snapshots of the fluid velocity field at the time instants  $t = 0.042, 0.168, 0.294, 0.42$  (from left to right and top to bottom). Algorithm 1 with  $r = 1$  and  $\tau = 4.2 \cdot 10^{-4}$ .

interface mid-point displacement and out-flow magnitudes are compared with the ones obtained with a first-order implicit coupling scheme. The impact of the extrapolations on the accuracy of Algorithm 1 is clear: very poor results are obtained for  $r = 0$ , reasonably good approximations are obtained with  $r = 1$  and for  $r = 2$  we retrieve the implicit coupling solution.

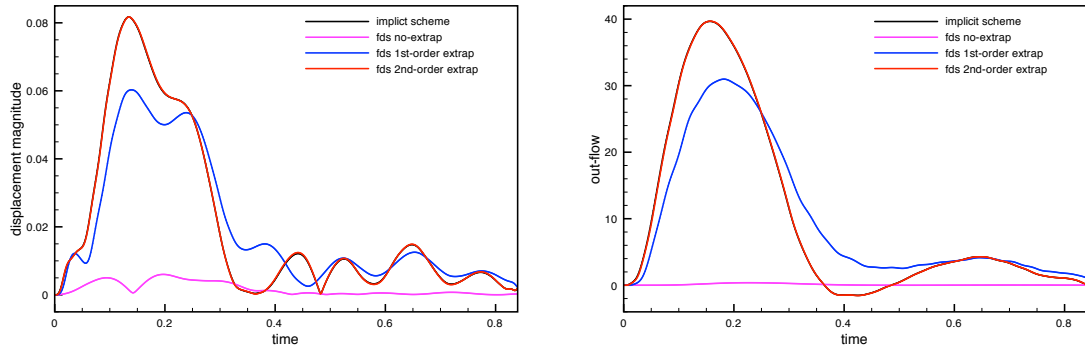


Figure 8: Comparison of the implicit and fully decoupled schemes: Left: Mid-point interface displacement. Right: Out-flow.

## 5.4 Damped structural instability

We consider the example proposed in [27] where an incompressible fluid is confined within two curved thin structures of different stiffness. The physical system is described by the non-linear coupled problem (1)-(2), with a Saint Venant-Kirchhoff constitutive relation for the (undamped)

shell. We take  $\rho^f = 1.0$  and  $\mu = 9$  in the fluid problem and  $\rho^s = 500$ ,  $\epsilon = 0.1$ ,  $E_{\text{top}} = 9 \cdot 10^5$ ,  $E_{\text{bottom}} = 9 \cdot 10^8$  and  $\nu = 0.3$  in the solid (the subscript notation indicates the bottom and top structures). The units are expressed in the SI system. On the left and right inflow boundaries, constant parabolic velocity profiles with maximal magnitudes 10 and 10.1 are, respectively, imposed. Homogeneous Dirichlet conditions are enforced on the remaining fluid boundaries. The volume force  $\mathbf{f} = (0, -1)^T$  loads the fluid.

We consider Algorithm 1 with the same spatial discretization than in the previous example. The simulations are carried out in three-dimensions by prescribing symmetry conditions on the extruded boundaries.

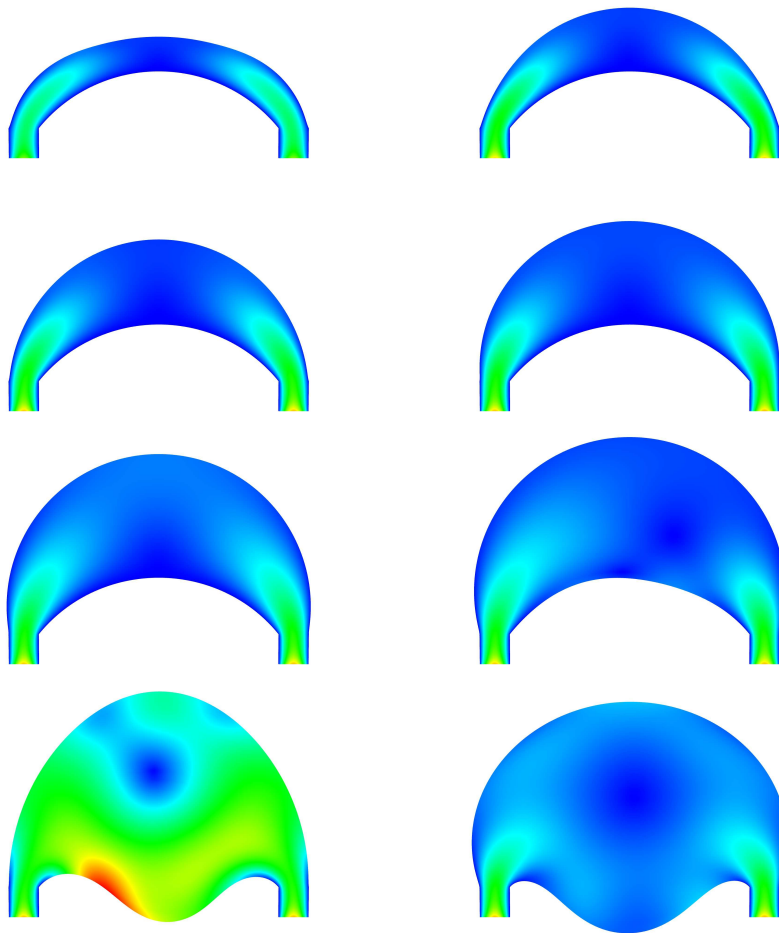


Figure 9: Snapshots of the fluid velocity at the time instants  $t = 0.5, 1, 1.5, 2, 2.5, 3, 3.5, 4$  (from left to right and top to bottom). Algorithm 1 with  $r = 1$ .

Figure 9 reports the fluid velocity magnitude at the time instants  $t = 0.5, 1, 1.5, 2, 2.5, 3, 3.5$  and  $4$ , using Algorithm 1 with  $r = 1$  and  $\tau = 0.005$ . We can clearly observe that the excess of fluid mass causes first the deflection of the upper (less stiff) structure. The fluid cavity continues to swell along the upper boundary until the fluid pressure reaches a critical level at

which the (stiffer) lower structure is no longer able to resist and collapses. A similar behavior was observed in [27], using an implicit scheme and an augmentation procedure which prescribes a volume constraint on the structural system.

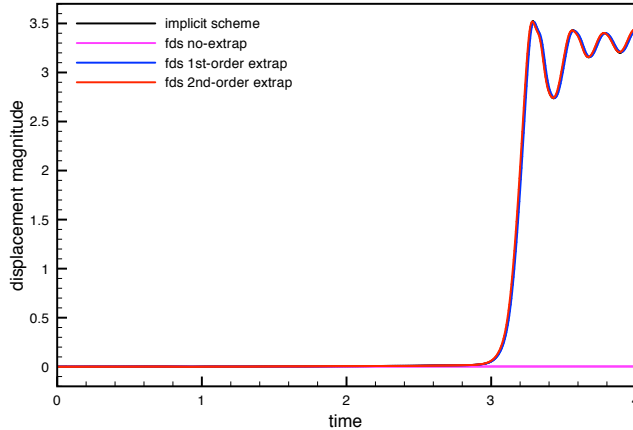


Figure 10: Comparison of the implicit and fully decoupled schemes: interface mid-point displacement magnitude of the bottom structure *vs.* time.

For comparison purposes, we have reported in Figure 10 the interface mid-point displacement magnitude of the lower structure obtained with Algorithm 1 (in its three extrapolated variants) and a first-order implicit scheme. The lack of accuracy for the scheme with  $r = 0$  is clearly visible one more time. Here, the unphysical excess of mass-loss across the interface impedes the collapse of the bottom structure. Conversely, the fully decoupled schemes with  $r = 1$  and  $r = 2$  are able to retrieve the numerical solution provided by the implicit scheme.

## 6 Conclusion

In this work we have introduced a new class of coupling schemes for fluid-structure interaction problems involving an incompressible fluid and a general thin-walled viscoelastic structure (*Reissner-Mindlin* shell). The methods proposed allow a fully decoupled time-marching of the complete fluid-solid state: fluid velocity, fluid pressure and solid displacement. The basic ingredients of this fluid-solid splitting paradigm are:

- fractional-step time-marching in the fluid (Chorin-Temam scheme);
- appropriate fractional-step time-marching of the interface Robin consistency (10), which yields explicit interface Robin conditions for the fluid sub-steps (only the solid inertia is treated implicitly);
- fluid stresses are transferred to the thin-walled structure in a standard fashion.

Unconditional stability has been proved for the variants with zeroth- and first-order extrapolation ( $r = 0, 1$ ) in a representative liner setting (Theorem 1). Though not covered by the stability analysis, numerical evidence has shown that the second-order extrapolation is stable for a reasonable range of the discretization parameters. The comprehensive numerical study

indicates also that the best accuracy and robustness is obtained with the first- and second-order extrapolated variants ( $r = 1, 2$ ). In particular, they retrieve the overall first-order accuracy of the fully implicit scheme.

Further investigation can be oriented in several directions. We can consider the extension to second-order time-marching schemes (e.g., via incremental pressure-correction in the fluid and overall second-order time-stepping), the analysis of the variant with second-order extrapolation and, more generally, the analysis in a fully discrete setting and the derivation of a priori error estimates. Another important problem, not covered by this study, is the case of the coupling with thick-walled solids. In this line, it is worth mentioning that the combination of the ideas reported in [16, 18] with the present coupling paradigm could spoil the first-order overall accuracy. Hence, alternative approaches will be explored.

## Acknowledgements

The authors are thankful to Marina Vidrascu for her support with the non-linear shell solver.

## References

- [1] M. Astorino, F. Chouly, and M. A. Fernández. Robin based semi-implicit coupling in fluid-structure interaction: Stability analysis and numerics. *SIAM J. Sci. Comput.*, 31(6):4041–4065, 2009.
- [2] M. Astorino and C. Grandmont. Convergence analysis of a projection semi-implicit coupling scheme for fluid-structure interaction problems. *Numer. Math.*, 116:721–767, 2010.
- [3] S. Badia, A. Quaini, and A. Quarteroni. Splitting methods based on algebraic factorization for fluid-structure interaction. *SIAM J. Sci. Comput.*, 30(4):1778–1805, 2008.
- [4] M. Bischoff, K.-U. Bletzinger, W.A. Wall, and E. Ramm. *Models and Finite Elements for Thin-Walled Structures*, chapter 3. John Wiley & Sons, Ltd, 2004.
- [5] M. Bukac, C. Canic, R. Glowinski, T. Tambaca, and A. Quaini. Fluid-structure interaction in blood flow capturing non-zero longitudinal structure displacement. *J. Comp. Phys.*, 235(0):515–541, 2013.
- [6] S. Čanić, J. Tambača, G. Guidoboni, A. Mikelić, C.J. Hartley, and D. Rosenstrauch. Modeling viscoelastic behavior of arterial walls and their interaction with pulsatile blood flow. *SIAM J. Appl. Math.*, 67(1):164–193, 2006.
- [7] P. Causin, J.-F. Gerbeau, and F. Nobile. Added-mass effect in the design of partitioned algorithms for fluid-structure problems. *Comput. Methods Appl. Mech. Engrg.*, 194(42–44):4506–4527, 2005.
- [8] D. Chapelle and K.J. Bathe. *The Finite Element Analysis of Shells - Fundamentals*. Springer, 2011.
- [9] A.J. Chorin. Numerical solution of the Navier-Stokes equations. *Math. Comp.*, 22:745–762, 1968.
- [10] J. Donéa, S. Giuliani, and J. P. Halleux. An arbitrary Lagrangian-Eulerian finite element method for transient dynamic fluid-structure interactions. *Comp. Meth. Appl. Mech. Engrng.*, pages 689–723, 1982.

- 
- [11] M. Eswaran, U.K. Saha, and D. Maity. Effect of baffles on a partially filled cubic tank: Numerical simulation and experimental validation. *Computers & Structures*, 87(3–4):198–205, 2009.
- [12] M.A. Fernández. Coupling schemes for incompressible fluid-structure interaction: implicit, semi-implicit and explicit. *SĕMA J.*, 55(1):59–108, 2011.
- [13] M.A. Fernández. Incremental displacement-correction schemes for incompressible fluid-structure interaction: stability and convergence analysis. *Numer. Math.*, 123(1):21–65, 2013.
- [14] M.A. Fernández, J.F. Gerbeau, and C. Grandmont. A projection semi-implicit scheme for the coupling of an elastic structure with an incompressible fluid. *Int. J. Num. Meth. Engrg.*, 69(4):794–821, 2007.
- [15] M.A. Fernández and M. Landajuela. A fully decoupled scheme for the interaction of a thin-walled structure with an incompressible fluid. *C. R. Math. Acad. Sci. Paris*, 351(3–4):161–164, 2013.
- [16] M.A. Fernández and J. Mullaert. Displacement-velocity correction schemes for incompressible fluid-structure interaction. *C. R. Math. Acad. Sci. Paris*, 349(17–18):1011–1015, 2011.
- [17] M.A. Fernández, J. Mullaert, and M. Vidrascu. Explicit Robin-Neumann schemes for the coupling of incompressible fluids with thin-walled structures. *Comput. Methods Appl. Mech. Engrg.*, 267:566–593, 2013.
- [18] M.A. Fernández, J. Mullaert, and M. Vidrascu. Generalized Robin-Neumann explicit coupling schemes for incompressible fluid-structure interaction: stability analysis and numerics. Research Report RR-8384, INRIA, 2013.
- [19] L. Formaggia, A. Quarteroni, and A. Veneziani, editors. *Cardiovascular Mathematics. Modeling and simulation of the circulatory system*, volume 1 of *Modeling, Simulation and Applications*. Springer, 2009.
- [20] C. Förster, W.A. Wall, and E. Ramm. Artificial added mass instabilities in sequential staggered coupling of nonlinear structures and incompressible viscous flows. *Comput. Methods Appl. Mech. Engrg.*, 196(7):1278–1293, 2007.
- [21] J.-L. Guermond. Some implementation of projection methods for Navier-Stokes equations. *M2AN Math. Model. Numer. Anal.*, 30:637–667, 1996.
- [22] J. L. Guermond, P. Mineev, and J. Shen. An overview of projection methods for incompressible flows. *Comput. Methods Appl. Mech. Engrg.*, 195(44–47):6011–6045, 2006.
- [23] G. Guidoboni, R. Glowinski, N. Cavallini, and S. Canic. Stable loosely-coupled-type algorithm for fluid-structure interaction in blood flow. *J. Comp. Phys.*, 228(18):6916–6937, 2009.
- [24] F. Hecht. New development in FreeFem++. *J. Numer. Math.*, 20(3–4):251–265, 2012.
- [25] M. Heil and A.L. Hazel. Fluid-structure interaction in internal physiological flows. In *Annual review of fluid mechanics. Volume 43, 2011*, volume 43 of *Annu. Rev. Fluid Mech.*, pages 141–162. Annual Reviews, 2011.
- [26] P. Kalita and R. Schaefer. Mechanical models of artery walls. *Arch. Comput. Methods Eng.*, 15(1):1–36, 2008.

- 
- [27] U. Küttler, C. Förster, and W.A. Wall. A solution for the incompressibility dilemma in partitioned fluid–structure interaction with pure Dirichlet fluid domains. *Comput. Mech.*, 38:417–429, 2006.
- [28] M. Lombardi, N. Parolini, A. Quarteroni, and G. Rozza. Numerical simulation of sailing boats: Dynamics, FSI, and shape optimization. In G. Buttazzo and A. Frediani, editors, *Variational Analysis and Aerospace Engineering: Mathematical Challenges for Aerospace Design*, Springer Optimization and Its Applications, pages 339–377. Springer, 2012.
- [29] M. Lukacova-Medvid’ovaa, G. Rusnakovaa, and A. Hundertmark-Zauskovaa. Kinematic splitting algorithm for fluid–structure interaction in hemodynamics. *Comput. Methods Appl. Mech. Engrg.*, 265(1):83–106, 2013.
- [30] P. Moireau, N. Xiao, M. Astorino, C. A. Figueroa, D. Chapelle, C. A. Taylor, and J-F. Gerbeau. External tissue support and fluid–structure simulation in blood flows. *Biomech. Model. Mechanobiol.*, 11:1–18, 2012.
- [31] F. Nobile and C. Vergara. An effective fluid–structure interaction formulation for vascular dynamics by generalized Robin conditions. *SIAM J. Sci. Comput.*, 30(2):731–763, 2008.
- [32] S. Oyre, E.M. Pedersen, S. Ringgaard, P. Boesiger, and W.P. Paaske. In vivo wall shear stress measured by magnetic resonance velocity mapping in the normal human abdominal aorta. *Eur. J. Vasc. Endovasc. Surg.*, 13:263–271, 1997.
- [33] M.P. Païdoussis, S.J. Price, and E. de Langre. *Fluid–structure interactions: cross-flow-induced instabilities*. Cambridge University Press, 2011.
- [34] A. Quaini and A. Quarteroni. A semi-implicit approach for fluid–structure interaction based on an algebraic fractional step method. *Math. Models Methods Appl. Sci.*, 17(6):957–983, 2007.
- [35] A.-V. Salsac, S.R. Sparks, J.M. Chomaz, and J.C. Lasheras. Evolution of the wall shear stresses during the progressive enlargement of symmetric abdominal aortic aneurysms. *J. Fluid Mech.*, 550:19–51, 2006.
- [36] K. Takizawa and T.E. Tezduyar. Computational methods for parachute fluid–structure interactions. *Arch. Comput. Methods Eng.*, 19:125–169, 2012.
- [37] R. Temam. Une méthode d’approximation de la solution des équations de Navier-Stokes. *Bull. Soc. Math. France*, 96:115–152, 1968.
- [38] D. Valdez-Jasso, H.T. Banks, M.A. Haider, D. Bia, Y. Zocalo, R.L. Armentano, and M.S. Olufsen. Viscoelastic models for passive arterial wall dynamics. *Adv. Appl. Math. Mech.*, 1(2):151–165, 2009.

## Contents

<b>1</b>	<b>Introduction</b>	<b>3</b>
<b>2</b>	<b>Problem setting</b>	<b>4</b>
<b>3</b>	<b>A class of fully decoupled schemes</b>	<b>5</b>
<b>4</b>	<b>Derivation and analysis in the linear case</b>	<b>6</b>
4.1	Time semi-discretization . . . . .	7
4.2	Stability analysis . . . . .	9
4.2.1	Preliminaries . . . . .	9
4.2.2	A priori energy estimate . . . . .	10
<b>5</b>	<b>Numerical experiments</b>	<b>13</b>
5.1	Convergence study in a two-dimensional test-case . . . . .	13
5.2	Pressure wave propagation in a straight tube . . . . .	16
5.3	Blood flow in an abdominal aortic aneurysm . . . . .	17
5.4	Damped structural instability . . . . .	18
<b>6</b>	<b>Conclusion</b>	<b>20</b>



**RESEARCH CENTRE  
PARIS – ROCQUENCOURT**

Domaine de Voluceau, - Rocquencourt  
B.P. 105 - 78153 Le Chesnay Cedex

Publisher  
Inria  
Domaine de Voluceau - Rocquencourt  
BP 105 - 78153 Le Chesnay Cedex  
[inria.fr](http://inria.fr)

ISSN 0249-6399